

GPUmonty: A GPU-accelerated relativistic Monte Carlo radiative transfer code

PEDRO NAETHE MOTTA ,¹ RODRIGO NEMMEN ,¹ AND ABHISHEK V. JOSHI ,²

¹*Instituto de Astronomia, Geofísica e Ciências Atmosféricas, Universidade de São Paulo, São Paulo, SP 05508-090, Brazil.*

²*Department of Physics, University of Illinois, 1110 West Green Street, Urbana, IL 61801, USA*

ABSTRACT

We introduce **GPUmonty**, a CUDA/C-based Monte Carlo radiative transfer code accelerated using graphics processing units (GPUs). **GPUmonty** derives from the CPU-based code **grmonty** and offloads the most computationally expensive stages of the calculation—superphoton generation, sampling, tracking, and scattering—to the GPU. Whereas **grmonty** handles photons sequentially, **GPUmonty** processes large numbers of superphotons concurrently, leveraging the single-instruction, multiple-thread (SIMT) execution model of modern GPUs. Benchmarks demonstrate a speedup of about $12\times$ relative to the original CPU implementation on a single GPU, with runtime limited primarily by register pressure rather than compute or memory bandwidth saturation. We validate the implementation through analytic tests for a optically thin synchrotron sphere, as well as comparisons with **igrmonty** for scattering synchrotron sphere and GRMHD simulation data. Relative errors remain below a percent level and convergence is consistent with the expected $N_s^{-1/2}$ Monte Carlo scaling. By significantly reducing computational costs, **GPUmonty** enables the extensive parameter space surveys and faster spectra modeling required to interpret horizon-scale observations of supermassive black holes. **GPUmonty** is publicly available under the GNU General Public License.

1. INTRODUCTION

To connect the multitude of multiwavelength observations of accreting black holes with their physics and perform parameter estimation, we need to model the electromagnetic spectrum that emerges from the hot gas flowing in a curved spacetime. There are a number of techniques for doing so. The two main techniques involve solving the radiative transfer equation and postprocessing snapshots of the fluid and magnetic field quantities generated from general relativistic magnetohydrodynamic (GRMHD) simulations (e.g. Wong et al. 2022)

The workhorse method for generating images and spectra in the radio and sub-millimeter regime relevant for VLBI imaging of Sgr A* or M87* (Event Horizon Telescope Collaboration et al. 2019a, 2022a; hereafter EHTC) is backward ray tracing. Here, instead of tracking every photon—most of which never reach the observer—we define a virtual “camera” far from the black hole. The trajectory of the rays are calculated backwards from each pixel of the camera toward the black hole horizon. Examples of ray tracing implementations of this observer-to-emitter include **ipole**

(Mościbrodzka & Gammie 2018), **BHOSS** (Younsi et al. 2012), **Jipole** (Naethe Motta et al. 2025) and **GRay** (Chan et al. 2013). Backward ray tracing struggles when there is significant scattering—relevant when modeling hard X-ray emission from accretion flows or gamma-ray production in relativistic jets. In such cases, the standard technique is Monte Carlo. Here, we generate probabilistically superphotons—packets representing many photons—throughout the flow based on the local emissivity. The gold standard implementation of this method is **grmonty** (Dolence et al. 2009), on which this work is based. Other examples include **Pandurata** (Schnittman & Krolik 2013), the multi-CPU **grmonty** extension **κ monty** (Davelaar et al. 2023), and **RAIKOU** (Kawashima et al. 2023), which uses the observer-to-emitter formalism to generate images and the reverse procedure to generate spectra

While recent efforts have focused on accelerating synthetic image generation in the context of Event Horizon Telescope observations (Palumbo et al. 2022; Tiede 2022; Moscibrodzka & Yfantis 2023; Sharma et al. 2025; Chang 2024; Yfantis et al. 2024; Keeble et al. 2025; Naethe Motta et al. 2025), multiwavelength spectral calculations—central to constraining models across the electromagnetic spectrum—have received comparatively little attention. Forward-modeling libraries now contain millions of snapshots (60,000 in EHTC M87* V; 5.5 mil-

Corresponding author: Pedro Naethe Motta
 Email: pedronaethemotta@usp.br

lion in EHTC Sgr A* V), yet Monte Carlo radiative transfer remains computationally prohibitive for more detailed analyses: spectra were computed for only 20% of the M87* images produced in EHTC M87* V, owing to the computational expense associated with sampling the large parameter space spanning observer inclinations, electron heating prescriptions, and emission models. As a result, Bayesian Monte Carlo Markov chain posterior sampling—now routine for image-based forward modeling—remains impractical for spectral calculations with existing codes. These demands will only intensify with more stringent probes of black hole environment with next-generation instruments such as the ngEHT (Johnson et al. 2023) and space-VLBI missions (Johnson et al. 2024) with their significantly improved angular resolution, dynamic range and cadence, further increasing library sizes and computational costs.

To harness the massively parallel computational power of GPUs for multiwavelength spectral calculations and address the computational bottlenecks previously described, we present **GPUmonty**: a relativistic radiative transfer code developed in C/CUDA based on the framework of the Monte Carlo code **grmonty**. By exploiting the modern hardware of NVIDIA GPUs, **GPUmonty** achieves over 12× speedup compared to **grmonty**.

This paper is organized as follows: In Section 2, we provide the governing equations and numerical methods used in **GPUmonty**. Section 3 describes the implementation of the GPU-accelerated algorithm and the main changes performed when porting **grmonty**. In Section 4, we validate the reliability of **GPUmonty** by performing three different tests: a uniform optically thin synchrotron sphere, a scattering synchrotron sphere test, and comparing spectra generated with **GPUmonty** and **grmonty** from a GRMHD simulation. In Section 5, we present a discussion of the code’s performance. Finally, in Section 6 we present the conclusions and future perspectives.

2. GOVERNING EQUATIONS AND NUMERICAL METHODS

2.1. Creation of superphotons

We follow the methods used in **grmonty** and treat the photon field as a collection of photon packets (so called superphotons), with a weight w representing the number of photons within each packet. The relation between superphotons and physical photons is given by $dN = wdN_s$, where N_s is the number of superphotons and N is the number of photons. The weight $w(\nu)$ is calculated as a function of the photon frequency ν in the plasma frame. The probability distribution for the superphotons can be written in terms of the weight w ,

frequency ν and emissivity j_ν as

$$\frac{1}{\sqrt{-g}} \frac{dN_s}{d^3x dt d\nu d\Omega} = \frac{1}{w\sqrt{-g}} \frac{dN}{d^3x dt d\nu d\Omega} = \frac{1}{w} \frac{j_\nu}{h\nu}. \quad (1)$$

Here, g is the determinant of the metric, dt is a differential time element, $d\Omega$ the differential solid angle, $d\nu$ the frequency interval, d^3x the volume element, and h is Planck’s constant. The final spectrum is divided into energy bins, and the corresponding weight for each energy bin can be expressed as

$$w_\nu(\nu) = \frac{\Delta t \Delta \ln \nu}{h N_s} \int \sqrt{-g} d^3x \int j_\nu d\Omega. \quad (2)$$

In practice, the computational domain is a grid and superphotons are generated independently in each zone considering the local plasma properties, with weights assigned according to the expected contribution of that zone to the final spectrum as given by Eq. 2. In **GPUmonty**, the total number of superphotons is controlled by the parameter N_s , which specifies the target number of superphotons to be generated by it; the actual number produced may differ slightly due to the stochastic sampling procedure but typically remains of the same order of magnitude.

2.2. Emissivity

In **GPUmonty**, we currently consider only thermal synchrotron emissivity, appropriate for the hot, optically thin accretion flows relevant to the systems studied here, following Leung et al. (2011). The emissivity j_ν is defined as

$$j_\nu(\nu, \theta) = \frac{\sqrt{2}\pi e^2 n_e \nu_s}{3c K_2(1/\Theta_e)} (X^{1/2} + 2^{11/12} X^{1/6})^2 \times \exp(-X^{1/3}), \quad (3)$$

where $X \equiv \nu/\nu_s$,

$$\nu_s = \frac{2}{9} \left(\frac{eB}{2\pi m_e c} \right) \Theta_e^2 \sin \theta, \quad (4)$$

θ is the angle between the magnetic field and the wave vector and $\Theta_e = k_b T_e / (m_e c^2) \gtrapprox 0.5$.

In the large temperature limit, for numerical stability we approximate $K_2(1/\Theta_e) \sim 2\Theta_e^2$ without any significant loss in accuracy.

2.3. Sampling procedure

The number of superphotons in zone i follows

$$N_{s,i} = \Delta t \Delta^3 x \sqrt{-g} \int \int d\nu d\Omega \frac{1}{w} \frac{j_\nu}{h\nu}. \quad (5)$$

These superphotons are distributed over frequency following the distribution

$$\frac{dN_{s,i}}{d\ln \nu} = \Delta t \Delta^3 x \sqrt{-g} \frac{1}{h w} \int d\Omega j_\nu, \quad (6)$$

and each superphoton is assigned a frequency by rejection sampling. We start by defining the maximum and minimum frequencies (ν_{\max}, ν_{\min} , respectively) before running the simulation. A random number, rand_1 , is drawn from the interval $[0, 1)$. The frequency is then chosen using the formula:

$$\nu_0 = \exp \left[\text{rand}_1 \ln \left(\frac{\nu_{\max}}{\nu_{\min}} \right) + \ln \nu_{\min} \right] \quad (7)$$

Next, a second random number rand_2 is drawn and the process repeats until the desired condition is met:

$$\text{rand}_2 < \frac{\left(\frac{dN_{s,i}}{d\ln \nu} \right)_{\nu_0}}{\max \left(\frac{dN_{s,i}}{d\ln \nu} \right)}. \quad (8)$$

Afterwards, we sample the photon direction by rejection sampling again. A preliminary value for θ is selected by sampling $\cos \theta = (2\text{rand}_3 - 1)$ from a uniform distribution over the range $[-1, 1)$. Next, a second random variable rand_4 is drawn from a uniform distribution over $[0, 1)$. The proposed value of θ is accepted if

$$\text{rand}_4 < \frac{j_\nu(\theta)}{j_\nu(\pi/2)}. \quad (9)$$

2.4. The geodesic equation

The superphotons created will follow null geodesics that can be described by the following set of first-order differential equations

$$\begin{aligned} \frac{dx^\mu}{d\lambda} &= k^\mu, \\ \frac{dk^\mu}{d\lambda} &= -\Gamma_{\alpha\beta}^\mu k^\alpha k^\beta, \end{aligned} \quad (10)$$

where x^μ is the four-position of the superphoton, k^μ is the four-velocity, λ is the affine parameter, and $\Gamma_{\alpha\beta}^\mu$ are the Christoffel symbols.

To solve the system of equations (10), we use the Velocity Verlet algorithm, a second-order numerical integration method (Swope et al. 1982). The algorithm updates the positions using the current velocities and accelerations, then computes the new accelerations and updates the velocities by averaging the old and new accelerations. In the context of Eq. 10, the algorithm

obeys

$$x_{n+1}^\mu = x_n^\mu + k_n^\mu \delta\lambda + \frac{1}{2} \left(\frac{dk^\mu}{d\lambda} \right)_n, \quad (11)$$

$$k_{n+1,p}^\mu = k_n^\mu + \left(\frac{dk^\mu}{d\lambda} \right)_n \delta\lambda, \quad (12)$$

$$\left(\frac{dk^\mu}{d\lambda} \right)_{n+1} = -\Gamma_{\alpha\beta}^\mu |_{(\text{at } x_{n+1})} k_{n+1,p}^\alpha k_{n+1,p}^\beta, \quad (13)$$

$$k_{n+1}^\mu = k_n^\mu + \frac{1}{2} \left[\left(\frac{dk^\mu}{d\lambda} \right)_n + \left(\frac{dk^\mu}{d\lambda} \right)_{n+1} \right] \delta\lambda, \quad (14)$$

where n is the step and $\delta\lambda$ is the step size. Here, $k_{n+1,p}^\mu$ represents the predicted velocity at step $n+1$. This prediction is necessary because the change in the wavevector is dependent on the wavevector itself. GPUmonty uses the calculated value from equation 14 to evaluate equation 12. This process is repeated until the relative error

$$\epsilon_{\text{err}} = \frac{|k_{n+1}^\mu - k_{n+1,p}^\mu|}{k_{n+1}^\mu} \quad (15)$$

is smaller than a configurable parameter of the implementation, which we set to 10^{-3} .

2.5. Covariant equation of radiative transfer

To account for the interaction of matter and photons along the geodesics, we use the covariant form of the unpolarized radiative transfer equation (Mihalas & Mihalas 1984; Younsi et al. 2012):

$$\mathcal{C} \frac{d}{d\lambda} \left(\frac{I_\nu}{\nu^3} \right) = \left(\frac{j_\nu}{\nu^2} \right) - (\nu \alpha_\nu) \left(\frac{I_\nu}{\nu^3} \right), \quad (16)$$

where α_ν is the frequency dependent absorption coefficient evaluated in the fluid frame. For thermal synchrotron, the absorption coefficient is defined as $\alpha_\nu = j_\nu/B_\nu$. We use the constant $\mathcal{C} \equiv h\ell/m_e c^2$ in units of cm s to convert $d\lambda$ from code to physical units, where ℓ is the length unit and h is Planck's constant in CGS. The specific intensity is proportional to the superphoton weight and is defined as

$$I_\nu = \frac{h\nu dN}{dA dt d\nu d\Omega} = \frac{h\nu w dN_s}{dA dt d\nu d\Omega} \propto w. \quad (17)$$

At each step of the geodesic integration, absorption and scattering are taken into account as described in the following sections.

2.6. Absorption

GPUmonty handles absorption by decreasing the weight w of the superphotons at each step of the geodesic integration as they travel through a medium. From the

radiative transfer equation (Eq. 16) and ignoring emission ($j_\nu = 0$), the evolution of the superphoton weight due to absorption is given by

$$\frac{dw}{d\tau_a} = -w; \quad (18)$$

where the optical depth for absorption is $d\tau_a = \nu\alpha_\nu C d\lambda$. Integrating Equation 18, the weight of each superphoton evolves as

$$w_{n+1} = w_n e^{-\tau_a}. \quad (19)$$

To improve accuracy, the absorption optical depth over a single step is computed by averaging the invariant absorption coefficient at the previous and current positions as

$$\tau_a = \frac{1}{2} [(\nu\alpha_\nu)_n + (\nu\alpha_\nu)_{n+1}] C \Delta\lambda, \quad (20)$$

2.7. Scattering

As superphotons propagate through the medium, we also account for potential scatterings. We model these using the probability distribution

$$p = 1 - e^{-b\tau_s} \quad (21)$$

where τ_s represents the scattering optical depth and b is the bias parameter with $b \geq 1$, as discussed in Kahn (1950); Dolence et al. (2009). The inclusion of b is essential for enhancing the number of superphotons that experience scattering in optically thin scenarios, increasing the signal-to-noise ratio in scattering-dominated situations. When a scattering happens, a new superphoton

is generated and we conserve the number of photons by setting the weight of the existing photon $w \rightarrow w(1-1/b)$ and the weight of the generated superphoton as w/b , such that $w(1-1/b) + w/b = 1$.

We account for the rate of interactions between photons and particles of mass m by taking into account the cross-section invariance (equation 12.7 in Landau & Lifschits 1975; Dolence et al. 2009)

$$\frac{1}{\sqrt{-g}} \frac{dN_{m\gamma}}{d^3x dt} = \int \frac{d^3p}{\sqrt{-gp^t}} \frac{dn_m}{d^3p} \frac{(-k_\mu p^\mu)}{k^t} \sigma c \quad (22)$$

where σ is the cross section and $dn_m = dN_m/d^3x$. It is possible to define a “hot cross section” as

$$\sigma_h = \frac{1}{n_m} \int d^3p \frac{dn_m}{d^3p} (1 - \mu_m \beta_m) \sigma, \quad (23)$$

where β is the particle speed and μ_m is the cosine of the angle between particle and photon momentum in the fluid frame (all quantities defined in the fluid frame). The extinction coefficient is

$$\alpha_\nu^{\text{sc}} = n_m \sigma. \quad (24)$$

Hence, we calculate the scattering optical depth analogously to the absorption optical depth in equation 20

$$\tau_{\text{sc}} = \frac{1}{2} [(\nu\alpha_\nu^{\text{sc}})_n + (\nu\alpha_\nu^{\text{sc}})_{n+1}] C \Delta\lambda. \quad (25)$$

In GPUmonty, σ_h is calculated a priori and stored in a lookup table. We adopt the Klein-Nishina total cross section,

$$\sigma_{\text{KN}} = \begin{cases} \sigma_T \frac{3}{4\epsilon_e^2} \left[2 + \frac{\epsilon_e^2(1+\epsilon_e)}{(1+2\epsilon_e)^2} + \frac{\epsilon_e^2-2\epsilon_e-2}{2\epsilon_e} \log(1+2\epsilon_e) \right], & \text{general case} \\ \sigma_T(1-2\epsilon), & \text{for } \epsilon \ll 1. \end{cases} \quad (26)$$

Numerically, to account for a scattering, we draw a random number $x_1 = -\log(\text{rand})$, calculate the bias parameter and then check if $bd\tau_{\text{scat}} > x_1$ is satisfied. If this is the case, the scattering takes place.

A plasma-frame orthonormal tetrad is constructed via a Gram–Schmidt orthogonalization procedure, and the wave vector of the incoming superphoton is transformed to this frame. The four-momentum of the scattering electron is sampled from the local electron distribution function using a rejection-sampling method following the approach implemented in **igrmonty** (Wong

et al. 2022). **igrmonty** is a modern implementation of **grmonty** maintained by the University of Illinois³. For each candidate electron–photon pair, a second rejection step to sample the scattered superphoton based on the differential Compton scattering cross section, using the Thomson limit at low photon energies and the full Klein–Nishina cross section otherwise. This procedure is equivalent to the prescription of Canfield et al.

³ Available for download at <https://github.com/AFD-Illinois/igrmonty>.

(1987) for isotropic thermal (Maxwell–Jüttner) electron distributions, but is more general and can be straightforwardly extended to non-thermal distribution functions. The scattered photon wave vector is finally constructed in the electron rest frame and boosted back to the coordinate frame.

3. IMPLEMENTATION OF THE GPU-ACCELERATED ALGORITHMS

GPUmonty is developed in CUDA/C, leveraging OpenMP for CPU tasks while primarily operating on the GPU. We use device link-time optimization (dlto) to optimize function calls, in-lining, and memory usage throughout the program.

We use the well-established CUDA library cuRAND to implement the pseudo-random number generator XORWOW, which boasts a period of $2^{192} - 2^{32}$. By “period” we mean the length of the sequence of random numbers that the generator can produce before it begins to repeat. In the case of XORWOW, the period is slightly less than 2^{192} .

GPUmonty uses five main kernels (global functions) for photon creation, sampling, tracking, scattering, and recording. CPU-side tasks are limited to creating tables and reading data from external files, such as plasma properties from GRMHD snapshots, computing the metric determinant for each zone when calculating the weight for photon emission, and generating the output spectrum. We also minimize data transfer between GPU and CPU memories, so that PCIe bandwidth is not a concern. Most data transfer occurs before the creation of superphotons, primarily involving the transfer of table values and global variables. After the superphotons are recorded for the final spectrum, their data is transferred back from the GPU to the CPU.

We generate, sample and track all superphotons at the same time, instead of generating them one by one as in **grmonty**. This minimizes the usage of atomic operations to global variables and also favors the Single Instruction Multiple Threads (SIMT) behavior of GPUs where threads are grouped into warps, and the same instruction is dispatched to all threads in a warp.

For photon generation, we employ stride-based parallelism, in which each GPU thread processes multiple plasma zones. Each thread is assigned a unique starting zone index equal to its global thread index. The thread then iterates over the domain by incrementing this index by a fixed stride equal to the total number of threads launched in the kernel. In this way, thread 0 processes zones $0, N_{\text{threads}}, 2N_{\text{threads}}, \dots$, thread 1 processes zones $1, 1+N_{\text{threads}}, 1+2N_{\text{threads}}, \dots$, and so on, ensuring that all plasma zones are covered exactly once.

For photon sampling and tracking, we use a different parallelism method. In this approach, each photon is assigned to a dedicated thread. Instead of using a fixed increment for each thread, the remaining photons are dynamically allocated as threads finish processing their assigned photons. This strategy is more efficient than stride-based parallelism because the time required for each photon to complete varies due to the rejection sampling method for the sampling methods described in Sec. 2.3, as well as due to different geodesics for different photons. As a result, threads that complete their tasks early are immediately reassigned to new photons, avoiding idle time while other threads finish processing.

In **grmonty**, photon scattering is handled through a recursive procedure, which is typically not ideal for GPUs due to their limited stack size. To overcome this limitation, we implemented an array of structures to store the properties of the scattered photons. These photons are then processed only after all original photons have been tracked. The scattering kernel manages this subsequent processing, allowing for multiple layers of scattering. Once all scattering events have been completed and recorded, the resulting spectrum data are transferred from device to host memory, and the output is written to a binary file.

Handling all the superphotons simultaneously has the downside of memory limitations, as it requires keeping track of every photon simultaneously in GPU memory. To overcome this, we first evaluate the available GPU memory and then divide the total number of superphotons into manageable batches that are executed serially. Each batch only saves the contribution of photons that achieved the recording criterion (not the photons themselves), i.e. the quantities entering the final observables, such as the superphoton weight, luminosity, energy, accumulated optical depths, scattering counts, and the detector bin. Therefore, the memory usage across batches is small. This algorithm allows us to free the memory of the processed superphotons before starting a new batch.

4. TESTS

In this section, we present the tests performed to validate our code. The three tests performed are: (1) optically thin synchrotron sphere, (2) scattering in an uniform synchrotron sphere, and (3) comparison between **igrmonty** and **GPUmonty** for a GRMHD simulation.

For the tests, we quantify the relative error between our method and the baseline as

$$\delta L = \frac{L_{\nu}^{\text{ref}} - L_{\nu}^{\text{ours}}}{L_{\nu}^{\text{ref}}}, \quad (27)$$

where “ours” and “ref” indicate **GPUmonty** and the corresponding baseline, respectively. The convergence pa-

rameter is defined as

$$\epsilon_{\text{err}} = \frac{1}{\Delta \log(\nu)} \int \frac{|L_{\nu}^{\text{ref}} - L_{\nu}^{\text{ours}}|}{L_{\nu}^{\text{ref}}} d \log \nu. \quad (28)$$

where \log has base 10.

4.1. Optically thin synchrotron sphere

We begin the tests with a spherical synchrotron-emitting cloud in the optically thin regime, in flat space-time. In this setup, we consider a homogeneous, uniform spherical cloud with a radius of $R_{\text{sphere}} = 1$ cm. We consider a grid with internal coordinates as $x^{\mu} = [t, \log(r), \theta, \phi]$. The cloud consists of relativistic electrons with a dimensionless temperature $\Theta_e = 100$ and an electron number density $n_e = 10^{13} \text{ cm}^{-3}$. A vertical uniform magnetic field is considered, $B^z = 1$ G, which in our coordinates translates to

$$B^t = 0, \quad (29)$$

$$B^r = B_0 \cos \theta / r^2, \quad (30)$$

$$B^{\theta} = -B_0 \sin \theta / r, \quad (31)$$

$$B^{\phi} = 0, \quad (32)$$

with $B_0 = 1$ G. With the photon optical path and the angle between the electron velocity and the magnetic field as $L = 1 r_g$ and $\pi/2$ respectively at $\nu = 10^9$ Hz, we estimate the optical depth as $\tau = \alpha_{\nu} L \approx 10^{-4}$, confirming that the sphere is optically thin.

A 2D grid is initialized with a resolution of $8192 \times 128 \times 1$, with a maximum radius of $r_{\text{out}} = 10000$ cm. A high resolution in the radial direction is necessary to smooth the boundaries of the sphere. The polar angle is closed within the interval $[0, \pi]$. We set up $r_{\text{max}} = 3000$ cm as the radius at which to stop tracking and save the superphoton, and divide the energy in 2500 energy bins of size $\ln(h\nu/m_e c^2) = 0.01$ to accurately represent the rapidly varying high-end tail of the spectrum.

The results are compared with the angle-averaged emissivity $\hat{\epsilon}_{\nu}$ integrated over the volume of the sphere. Because the emissivity values are the same for every cell within the sphere, we can write

$$L_{\nu}^{\text{ref}} = \int \sqrt{-g} \hat{\epsilon}_{\nu} dV = \frac{4\pi R_{\text{sphere}}^3}{3} \hat{\epsilon}_{\nu}. \quad (33)$$

Figure 1 compares the fiducial analytical and simulated spectra considering $N_s = 10^8$. There is an excellent agreement between the numerical and analytical spectra, validated by the maximum difference between the numerical and analytical results remaining below 1% in all energy bins.

Figure 2 shows the normalized integrated error (eq. 27) as we vary the number of superphotons considering $N_s = [10^4, 10^5, 10^6, 10^7, 10^8]$. The convergence scales

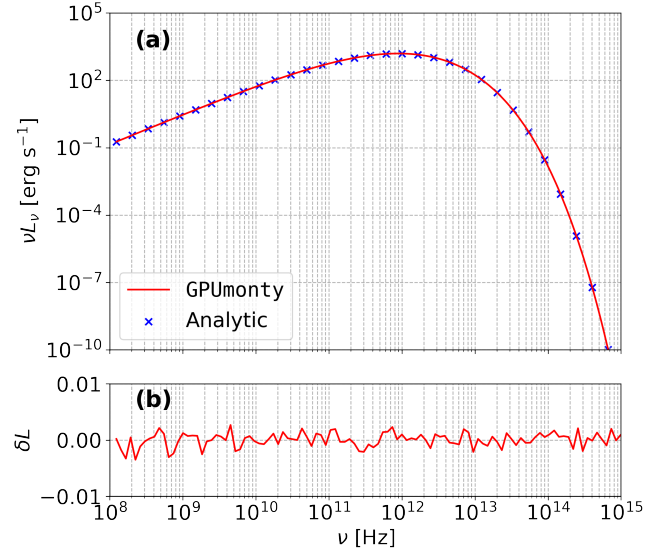


Figure 1. Panel (a): Optically thin synchrotron sphere spectrum considering $N_s = 10^8$. The red line represents the synthetic spectrum generated with GPUmonty and the purple markers are the analytical results from the angle-integrated emissivity calculated with equation (33). Panel (b): Residuals computed with equation (27).

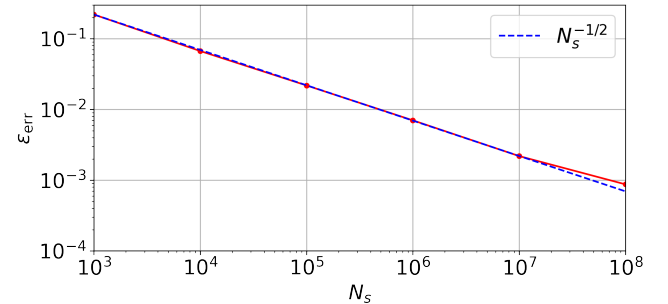


Figure 2. Normalized integrated error for different values of N_s , computed with equation (28). The blue dashed line represents the convergence $\epsilon_{\text{err}} \propto N_s^{-1/2}$ as expected in Monte Carlo simulations.

proportional to $1/\sqrt{N_s}$, as expected for the statistical error of a Monte Carlo estimator approaching the true underlying distribution. This result matches igrmonty's.

4.2. Scattering in an optically thick sphere

To validate the scattering algorithm, we consider the same uniform cloud of gas as described in Section 4.1 but this time with an electron density $n_e = 10^{18} \text{ cm}^{-3}$ and a dimensionless temperature of $\Theta_e = 3$. Only in the scattering test, to enhance the scattering, the bias parameter is adopted as

$$b = n_e \sigma_T R_{\text{sphere}} (n_{\text{sc}} + 1)^2, \quad (34)$$

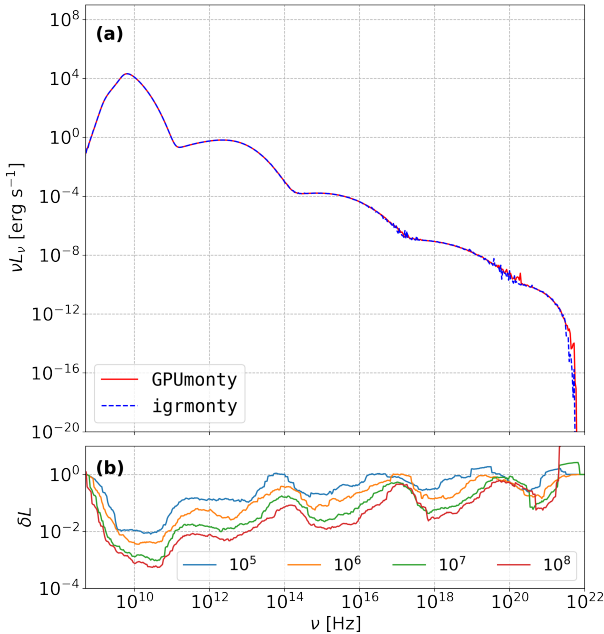


Figure 3. Panel (a): Scattering test for an uniformly spherical cloud of gas. The **GPUmonty** spectrum is shown with the red solid line and **igrmonty**’s with the blue dashed line, both with $N_s = 10^8$. Panel (b): The frequency-dependent residuals, computed as in Figure 1, for different values of N_s . For clarity, the curves have been smoothed using a moving average over the 10 nearest frequency bins.

where n_{sc} indicates the scattering generation of the photon. In other words, photons with $n_{sc} = 0$ are primary photons and the first scattered photons have $n_{sc} = 1$ etc. For this test, we allow for scatterings up to $n_{sc} = 4$.

Figure 3 shows the results from both **igrmonty** and **GPUmonty** for $N_s = 10^8$ where each bump corresponds to a different scattering. There is an excellent agreement between the two methods. The tails of each bump exhibit increased noise which becomes more pronounced with higher n_{sc} . This elevated noise originates from the tail of the preceding bump, whose photons generally carry smaller weights, making it difficult to fully suppress noise in these regions. This effect gets intensified with successive scatterings. As expected, as the number of superphotons increases the error decreases in the whole frequency domain except for the frequencies that match the end tail of each scattering round. The bottom panel of the figure shows the residuals where N_s is varied in **GPUmonty** and fix $N_s = 10^8$ in **igrmonty**.

Figure 4 shows the convergence parameter defined in Equation 28. For this test, the integration is carried out

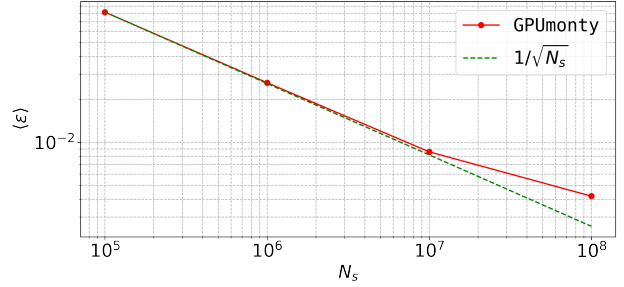


Figure 4. Normalized integrated error (equation (28)) for different N_s sizes. The green dashed line represents $\epsilon_{err} \propto N_s^{-1/2}$.

up to $\nu = 10^{15}$ Hz, since the large errors observed in the higher-scattering bumps are also present in **igrmonty**, and would otherwise distort the convergence rate. Eliminating these errors would require running **igrmonty** with a significantly larger number of superphotons.

4.3. GRMHD simulation

In this section, we use the GRMHD code **iham3d** (Prather et al. 2021) to simulate the accretion flow around a Kerr black hole. The snapshot used for the generation of the synthetic spectrum is the same one used for the EHT polarized radiative transfer code comparison (Prather et al. 2023)⁴.

The simulation is conducted in 3D with a resolution of $288 \times 128 \times 128$ elements and begins with a Fishbone & Moncrief (1976) torus in Standard And Normal Evolution (SANE) magnetic topology (Porth et al. 2019) with a $a_* = 0.9375$ spin. This simulation reflects the simulation dataset used in EHTC M87* V and Event Horizon Telescope Collaboration et al. (2021) (hereafter EHTC M87* VII). The simulation details are further detailed in Wong et al. (2022). The snapshot is taken at $4,500 r_g/c$ after the simulation starts, when the system reaches a quasi-steady accretion state in the inner disk regions. We consider a black hole of mass $M = 4.14 \times 10^6 M_\odot$ as appropriate for Sgr A* and a conversion factor from code units to CGS of $\mathcal{M} = 1 \times 10^{16}$ g.

For our analysis, the minimum frequency is set at 10^8 Hz and the maximum frequency at 10^{16} Hz for the synchrotron emission, with a minimum weight of $w = 10^{28}$. The energy bins are log-spaced, with a bin size defined by $\ln(h\nu/m_ec^2) = 0.12$, accounting for a total of 800 bins and starting the minimum energy bin at approximately 1.2×10^8 Hz. The bias factor is set at $b = 96 \times 10^4 \times \Theta_e^2$. Finally, we consider $N_s = 10^6$ and

⁴ The snapshot can be downloaded in [this link](#).

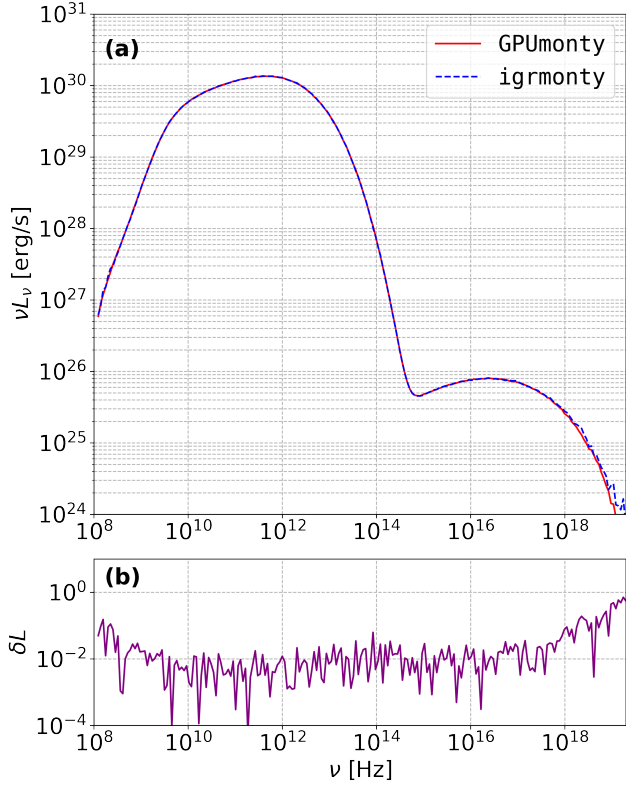


Figure 5. Panel (a): Comparison of spectra computed with **GPUmonty** (red solid line) and **igrmonty** (blue dashed line) for a 3D SANE accretion flow GRMHD simulation around a Kerr black hole. Both spectra use the same parameters and $N_s = 10^6$. Panel (b): Residuals computed as in Figure 1 with **igrmonty** as baseline.

allow only photons that reach $r > 1000 r_g$ to contribute to the recorded spectrum.

Figure 5 compares the spectra computed using the two radiative transfer codes for the selected GRMHD snapshot. The spectra agree closely over the full frequency range, with slight deviations only at the high-frequency tail, where the small number of scattered superphotons leads to Poisson noise. The error remains at the level of $\sim 10^{-2}$ across most frequencies and rises substantially only in the high-frequency tail for the aforementioned reason.

5. GPU BENCHMARK

In this section, the performance of our GPU-accelerated algorithm is evaluated. We rely on NVIDIA’s profiling tool **Nsight Compute**, which will provide all the metrics for this section.

The benchmarking is performed on the GRMHD simulation evaluated in Section 4.3. The GPU runs were executed on an NVIDIA A100 GPU with 40 GB of HBM2 memory in the SXM form factor, featuring 108 stream-

ing multiprocessors (SMs). CPU runs were performed on a single-socket AMD EPYC 7763 processor with 64 physical cores and 4 NUMA nodes. Each SM on the A100 can schedule up to 32 concurrent thread blocks, with a maximum of 1024 threads per block and a hardware limit of 2048 resident threads per SM. In our runs, we use 256 threads per block and a total number of blocks set to $108 \times 32 = 3456$, ensuring full occupancy of all SMs. Although **GPUmonty** is primarily GPU-driven, it relies on a few auxiliary CPU tasks as described in Section 3. In the **GPUmonty** runs, we optimize CPU-GPU affinity and minimize NUMA-related overheads by allocating 16 OpenMP threads binding them to the NUMA node local to the GPU. In the **igrmonty** runs, we use a full dedicated AMD7763 node with the all the 64 cores.

5.1. Runtime and speedup

The performance of **GPUmonty** and **igrmonty** is analyzed as a function of the number of superphotons, spanning $N_s = 10^3-10^9$. It is worth noting that the actual number of superphotons generated is usually larger than N_s by a factor of $\sim 7-10\times$. All results presented here correspond to the same bias parameter value as chosen in Section 4.3, since modifying this parameter would change the number of scattered superphotons generated and thus alter the workload of the scattering routine. This could systematically impact the run times.

The resulting execution times and speedup factors are depicted in Figure 6. We define the speedup factor as the ratio of **igrmonty** to **GPUmonty** execution time. Results are shown for a fixed bias parameter consistent with Section 4.3.

At low workloads corresponding to small photon numbers of $N_s \lesssim 10^4$, the execution times of our GPU code and the pure CPU method are comparable. The reason is that for small N_s , the overhead associated with GPU and CPU initialization and memory tasks (i.e. kernel launches, host-to-device data transfers; CPU-tasks such as data reading and table generation) is comparable to GPU computations related to photon generation and propagation. Once N_s increases, **GPUmonty** exhibits superior scaling compared to **igrmonty** due to our optimizations.

The speedup generally improves with the workload, reaching a maximum of approximately $12\times$. A slight drop in the speedup factor at $N_s = 10^7$ is noticeable, which is explained by the workload exceeding the available GPU RAM, requiring the simulation to be processed in two serialized batches rather than a single pass. The batching serialization impacts the efficiency, though the speedup recovers as the workload increases further. Since we expect **GPUmonty** to typically run

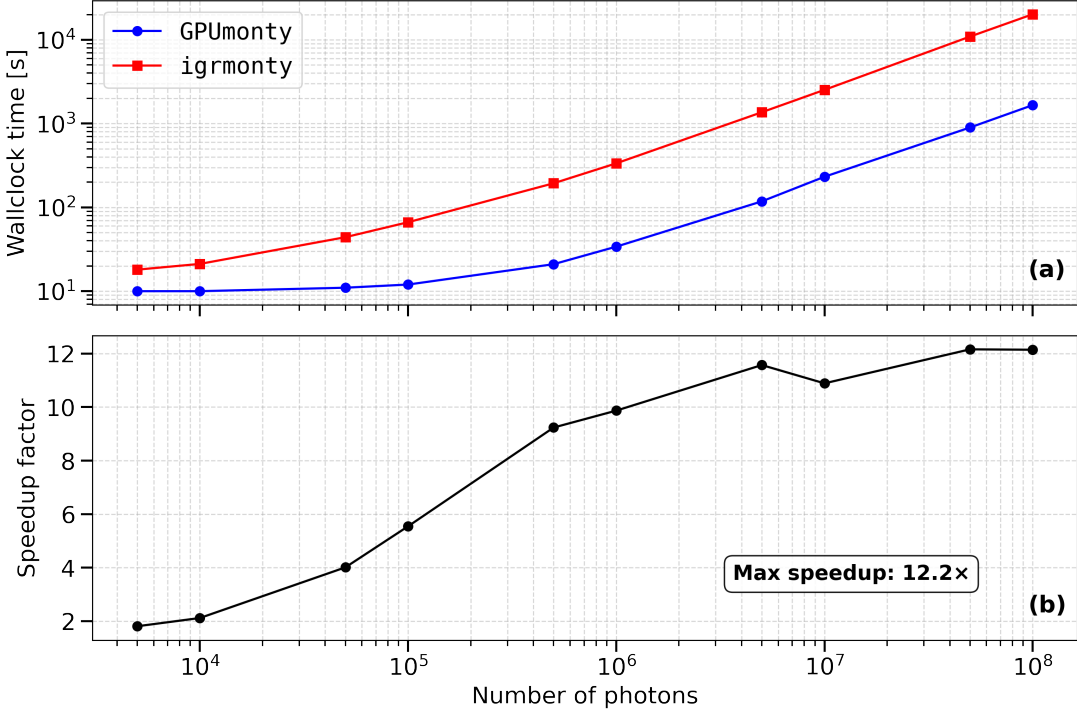


Figure 6. Panel (a): Performance comparison between **GPUmonty** and **igrmonty** (CPU-based) as a function of superphoton number N_s . Top panel: Wallclock time in seconds; **GPUmonty** in blue circles, **igrmonty** in red squares. Panel (b): Resulting speedup factor achieved by **GPUmonty** relative to **igrmonty**. The speedup peaks at a factor of ~ 12 as the workload increases.

with $N_s \gtrsim 10^6$ to ensure a high signal-to-noise ratio, **GPUmonty** effectively operates in the regime where the performance has already reached a plateau, providing a consistent speedup of approximately $12 \times$.

We also quantify the codes' performances for the most efficient setup, corresponding to $N_s = 5 \times 10^7$, by computing the number of processed superphotons per second. In the **GPUmonty** run, a total of 1,597,322,804 superphotons are generated, including both plasma-emitted and scattered photons, over a runtime of 898 seconds. This corresponds to a processing rate of approximately 1.78×10^6 superphotons/s. For the same value of N_s , the **igrmonty** run produces 1,433,396,661 superphotons with a total runtime of 10,906 seconds, yielding a processing rate of $\sim 1.31 \times 10^5$ superphotons/s.

Performance on consumer-grade hardware was also evaluated to assess the speedup achievable on personal machines. The comparison was carried out between an NVIDIA GeForce RTX 3050 Laptop GPU (4 GB VRAM) and a AMD Ryzen 5 6600H, using $N_s = 10^6$ in both cases. In this scenario, **GPUmonty** took 332 seconds to run, while **igrmonty** took 2,692 seconds, characterizing a solid speedup of $\sim 8 \times$. As expected, the speedup is hardware-dependent and may vary with the specific system configuration.

5.2. Kernel execution times and bottlenecks

For this analysis, the same setup is executed with $N_s = 10^6$. Table 1 reports metrics describing kernel execution time, compute throughput, memory and cache utilization, and SM occupancy, which together characterize how the kernel uses the GPU resources.

The kernel duration row shows that the total runtime is almost entirely dominated by the photon tracking stages. The superphoton tracking kernel alone accounts for 42% of the execution time, while scattered tracking contributes an additional 57%. This indicates that performance optimization efforts should focus on the tracking stages, as improvements in other kernels would have a negligible impact on the overall runtime. The relative cost of the scattered tracking kernel depends on the chosen bias parameter. For the run shown here, this parameter leads to a larger number of scattered to generated superphotons.

An important factor limiting performance in our current implementation is the theoretical occupancy of the GPU, which measures the fraction of a streaming multiprocessor's resources that can be actively used by warps given the kernel's register and shared memory usage. In our case, the kernels are relatively long and require a substantial number of registers per thread to minimize register spilling, which inherently reduces the theoretical

Table 1. GPU benchmarking metrics for different kernels in the simulation. Because some kernels are called more than one time, we report these parameters for the slowest execution of each kernel. The percentages enclosed by the parenthesis on the occupancy rows signals the theoretical occupancy for each kernel.

Metric	Generation	Sampling	Tracking	Scattered	Recording
Kernel Duration	0.30%	0.20 %	42.32%	57.05%	0.13%
Achieved/Theoretical Occupancy	95.2% (12.5%)	99.7% (12.5%)	100.0% (12.5%)	100.0% (12.5%)	95.2% (62.5%)
Compute Throughput	66.03%	57.99%	17.44%	17.98%	12.23%
Memory Throughput	6.83%	3.12%	24.69%	26.13%	24.19%

occupancy. In our tests, we found that reducing register pressure rather than maximizing occupancy actually led to shorter overall runtimes, making this trade-off beneficial for performance. While this means that not all hardware resources are fully used at all times, it allows each kernel to run efficiently without excessive memory access penalties. It is worth noting that this is an area where performance could be further optimized, and we plan to explore strategies to improve it in future work.

We find that prioritizing reduced register pressure over maximizing occupancy leads to improved performance. When forcing a lower register count (e.g. 32 registers per thread), the theoretical occupancy increases to 100%, with achieved occupancy exceeding 99.8% for the tracking kernels. However, under this configuration the overall runtime increases compared to the baseline case with 12.5% theoretical occupancy for most kernels, indicating that the increased register spilling and memory traffic outweigh the benefits of higher occupancy.

Achieving higher occupancy would require substantial refactoring of the code, potentially restructuring the algorithm into multiple smaller kernels. This may not be feasible given the inherently register-intensive nature of photon tracking. Despite these constraints, the current implementation still achieves a 12 \times speedup relative to the reference CPU version, demonstrating that GPU acceleration remains highly effective. Future work will explore strategies to further reduce register usage, such as minimizing local variables, although the intrinsic complexity of the tracking algorithm may continue to impose high register demands.

5.3. NVIDIA *Nsight Compute* metrics

Compute throughput varies significantly across kernels. The superphoton generation and sampling kernels achieve high throughputs of 66% and 58% respectively, indicating that these kernels consist largely of regular arithmetic operations with limited branching and good instruction-level parallelism. In contrast, the tracking kernels exhibit significantly lower compute throughput, with 18% for superphoton tracking and 22% for scat-

tered tracking. To determine if this low utilization was simply a byproduct of low occupancy (12.5%), we performed a stress test by capping the register count at 32 per thread.

This configuration achieved an occupancy of 99.9%, yet the compute throughput actually decreased to \sim 10%. Simultaneously, memory throughput surged to 68.9% due to massive register spilling to local memory. This result demonstrates that even when the GPU is fully saturated with active warps, the compute pipes remain under-utilized. This confirms that the low compute throughput is intrinsic to the photon transport algorithm, which is dominated by complex control flow, instruction latency, and special-function units rather than long, throughput-oriented arithmetic sequences.

Memory throughput shows an inverse trend compared to compute throughput. The early-stage kernels make minimal use of global memory bandwidth, with values below 7%, reflecting their usage of register-resident data and limited memory traffic. In contrast, the tracking and recording kernels reach memory throughput values between 24% and 31%. Although still well below saturation, these values indicate sustained interaction with global memory, driven by photon state updates, global spectrum variables recording and scattering bookkeeping. Importantly, all kernels operate well below the maximum available bandwidth, demonstrating that **GPUmonty** is not limited by memory bandwidth and that global memory access does not constitute the primary performance bottleneck. In the scenario of 32 register per thread limit, the tracking kernels reached a memory throughput of approximately 68%. While this represents a significant increase in data movement, it remained below the maximum theoretical bandwidth of the A100.

6. CONCLUSIONS

This paper introduces the GPU-accelerated general relativistic Monte Carlo radiative transfer code **GPUmonty**. It is designed to compute the electromagnetic spectra emitted by hot gas in accretion flows around black holes due to the synchrotron and inverse Compton

ton scattering processes. **GPUMonty** is a complete CUDA port of **grmonty**, making efficient use of NVIDIA GPUs via parallelism in five kernels: superphoton generation, sampling, tracking, scattering and recording. The original functions that relied on recursion, such as geodesic calculation and photon scattering, were restructured and optimized to accommodate the low stack size of GPUs.

GPUMonty is validated using three complementary tests designed to assess the accuracy of photon emission, absorption, and scattering: an optically thin synchrotron-emitting sphere and a self-synchrotron-Compton sphere in Minkowski spacetime, and a GRMHD simulation of a SANE radiatively inefficient accretion flow around a rapidly rotating black hole. Our benchmarks are, respectively, the corresponding analytical solution for the first test, and a **igrmonty** for the second and third ones. In all tests, an excellent agreement with the benchmark is found, validating the physical accuracy and expected Monte Carlo method statistical convergence of our GPU implementation. In our tests based on a GRMHD simulation, a 12× speedup is achieved using a single GPU when compared to **igrmonty**, a CPU-based fork of **grmonty**.

In future work, **GPUMonty** will be extended with additional physical processes, including bremsstrahlung emission, non-thermal electron distributions, and photon polarization. Future updates will also include a bias-tuning process, where we will be able to control the amount of scattered photons to mitigate noise on the fly. The explicit separation of scattered-photon tracking in **GPUMonty** is expected to enable the implementation of new bias-tuning algorithms compared to those employed in **igrmonty**. On the performance side, optimization opportunities identified in Section 5 will be further investigated. Particular emphasis will be placed on mitigating register pressure through kernel reorgani-

zation. Portability to non-NVIDIA GPU architectures using HIP-based programming models will also be explored to broaden hardware support.

ACKNOWLEDGEMENTS

PNM thanks Alejandro Cárdenas-Avendaño, Douglas Ferreira, Trevor Gravely and Ben Prather for useful discussions, Angelina Lesniak for assistance with the algorithmic development, Reinaldo Lima for help with the testing algorithms, and Charles Gammie for valuable comments and suggestions on the manuscript. RN thanks Matheus T. Bernardino and Alfredo Goldman for their work on an early phase of this project. PNM also acknowledges the Center for Nonlinear Studies (CNLS) at Los Alamos National Laboratory (LANL) for hosting discussions that contributed to this work. RN gratefully acknowledges Rafa Munoz for the generous gift of a GPU, used in this research. PNM acknowledges financial support from the Fundação de Amparo à Pesquisa do Estado de São Paulo (FAPESP) under grant number 2023/15835-2. RN acknowledges a Bolsa de Produtividade from Conselho Nacional de Desenvolvimento Científico e Tecnológico. This work used Delta CPU and GPU resources at the National Center for Supercomputing Applications (NCSA) through allocations PHY250391, PHY250091 and AST170024 from the Advanced Cyberinfrastructure Coordination Ecosystem: Services & Support (ACCESS) program, which is supported by U.S. National Science Foundation grants #2138259, #2138286, #2138307, #2137603, and #2138296.

DATA AVAILABILITY

GPUMonty is available on GitHub at <https://github.com/black-hole-group/gpumonty>, with documentation hosted at <https://black-hole-group.github.io/gpumonty/>. The project is released under the GNU GPL v2.0 license.

REFERENCES

Canfield, E., Howard, W. M., & Liang, E. P. 1987, *ApJ*, 323, 565, doi: [10.1086/165853](https://doi.org/10.1086/165853)

Chan, C.-k., Psaltis, D., & Öznel, F. 2013, *ApJ*, 777, 13, doi: [10.1088/0004-637X/777/1/13](https://doi.org/10.1088/0004-637X/777/1/13)

Chang, D. 2024, *Journal of Open Source Software*, 9, 7273, doi: [10.21105/joss.07273](https://doi.org/10.21105/joss.07273)

Davelaar, J., Ryan, B. R., Wong, G. N., et al. 2023, *MNRAS*, 526, 5326, doi: [10.1093/mnras/stad3023](https://doi.org/10.1093/mnras/stad3023)

Dolence, J. C., Gammie, C. F., Mościbrodzka, M., & Leung, P. K. 2009, *The Astrophysical Journal Supplement Series*, 184, 387, doi: [10.1088/0067-0049/184/2/387](https://doi.org/10.1088/0067-0049/184/2/387)

Event Horizon Telescope Collaboration, Akiyama, K., Alberdi, A., et al. 2019a, *ApJ*, 875, L1, doi: [10.3847/2041-8213/ab0ec7](https://doi.org/10.3847/2041-8213/ab0ec7)

Event Horizon Telescope Collaboration, Akiyama, K., Alberdi, A., et al. 2019b, *The Astrophysical Journal*, 875, L5, doi: [10.3847/2041-8213/ab0f43](https://doi.org/10.3847/2041-8213/ab0f43)

Event Horizon Telescope Collaboration, Akiyama, K., Algaba, J. C., et al. 2021, *The Astrophysical Journal Letters*, 910, L12, doi: [10.3847/2041-8213/abe71d](https://doi.org/10.3847/2041-8213/abe71d)

Event Horizon Telescope Collaboration, Akiyama, K., Alberdi, A., et al. 2022a, *ApJL*, 930, L12, doi: [10.3847/2041-8213/ac667410.3847/2041-8213/ac667510.3847/2041-8213/ac6429](https://doi.org/10.3847/2041-8213/ac667410.3847/2041-8213/ac667510.3847/2041-8213/ac6429)

Event Horizon Telescope Collaboration, Akiyama, K., Alberdi, A., et al. 2022b, *The Astrophysical Journal Letters*, 930, L16, doi: [10.3847/2041-8213/ac6672](https://doi.org/10.3847/2041-8213/ac6672)

Fishbone, L. G., & Moncrief, V. 1976, *ApJ*, 207, 962, doi: [10.1086/154565](https://doi.org/10.1086/154565)

Johnson, M. D., Akiyama, K., Blackburn, L., et al. 2023, *Galaxies*, 11, 61, doi: [10.3390/galaxies11030061](https://doi.org/10.3390/galaxies11030061)

Johnson, M. D., Akiyama, K., Baturin, R., et al. 2024, in *Society of Photo-Optical Instrumentation Engineers (SPIE) Conference Series*, Vol. 13092, *Space Telescopes and Instrumentation 2024: Optical, Infrared, and Millimeter Wave*, ed. L. E. Coyle, S. Matsuura, & M. D. Perrin, 130922D, doi: [10.1117/12.3019835](https://doi.org/10.1117/12.3019835)

Kahn, H. 1950, *Nucleonics*, 6, 60

Kawashima, T., Ohsuga, K., & Takahashi, H. R. 2023, *ApJ*, 949, 101, doi: [10.3847/1538-4357/acc94a](https://doi.org/10.3847/1538-4357/acc94a)

Keeble, L. S., Cárdenas-Avendaño, A., & Palumbo, D. C. M. 2025, *PhRvD*, 111, 103042, doi: [10.1103/PhysRevD.111.103042](https://doi.org/10.1103/PhysRevD.111.103042)

Landau, L. D., & Lifschits, E. M. 1975, *Course of Theoretical Physics*, Vol. Volume 2, *The Classical Theory of Fields* (Oxford: Pergamon Press)

Leung, P. K., Gammie, C. F., & Noble, S. C. 2011, *ApJ*, 737, 21, doi: [10.1088/0004-637X/737/1/21](https://doi.org/10.1088/0004-637X/737/1/21)

Mihalas, D., & Mihalas, B. W. 1984, *Foundations of radiation hydrodynamics*

Mościbrodzka, M., & Gammie, C. F. 2018, *MNRAS*, 475, 43, doi: [10.1093/mnras/stx3162](https://doi.org/10.1093/mnras/stx3162)

Moscibrodzka, M. A., & Yfantis, A. I. 2023, *The Astrophysical Journal Supplement Series*, 265, 22, doi: [10.3847/1538-4365/acb6f9](https://doi.org/10.3847/1538-4365/acb6f9)

Naethe Motta, P., Prather, B. S., & Cárdenas-Avendaño, A. 2025, *The Astrophysical Journal*, 995, 56, doi: [10.3847/1538-4357/ae16a0](https://doi.org/10.3847/1538-4357/ae16a0)

Palumbo, D. C. M., Gelles, Z., Tiede, P., et al. 2022, *The Astrophysical Journal*, 939, 107, doi: [10.3847/1538-4357/ac9ab7](https://doi.org/10.3847/1538-4357/ac9ab7)

Porth, O., Chatterjee, K., Narayan, R., et al. 2019, *The Astrophysical Journal Supplement Series*, 243, 26, doi: [10.3847/1538-4365/ab29fd](https://doi.org/10.3847/1538-4365/ab29fd)

Prather, B., Wong, G., Dhruv, V., et al. 2021, *The Journal of Open Source Software*, 6, 3336, doi: [10.21105/joss.03336](https://doi.org/10.21105/joss.03336)

Prather, B. S., Dexter, J., Mościbrodzka, M., et al. 2023, *The Astrophysical Journal*, 950, 35, doi: [10.3847/1538-4357/acc586](https://doi.org/10.3847/1538-4357/acc586)

Schnittman, J. D., & Krolik, J. H. 2013, *ApJ*, 777, 11, doi: [10.1088/0004-637X/777/1/11](https://doi.org/10.1088/0004-637X/777/1/11)

Sharma, A., Medeiros, L., Wong, G. N., et al. 2025, *Astrophys. J.*, 985, 40, doi: [10.3847/1538-4357/adc104](https://doi.org/10.3847/1538-4357/adc104)

Swope, W. C., Andersen, H. C., Berens, P. H., & Wilson, K. R. 1982, *The Journal of Chemical Physics*, 76, 637, doi: [10.1063/1.442716](https://doi.org/10.1063/1.442716)

Tiede, P. 2022, *Journal of Open Source Software*, 7, 4457, doi: [10.21105/joss.04457](https://doi.org/10.21105/joss.04457)

Wong, G. N., et al. 2022, *Astrophys. J. Supp.*, 259, 64, doi: [10.3847/1538-4365/ac582e](https://doi.org/10.3847/1538-4365/ac582e)

Yfantis, A. I., Mościbrodzka, M. A., Wielgus, M., Vos, J. T., & Jimenez-Rosales, A. 2024, *Astronomy & Astrophysics*, 685, A142, doi: [10.1051/0004-6361/202348230](https://doi.org/10.1051/0004-6361/202348230)

Younsi, Z., Wu, K., & Fuerst, S. V. 2012, *Astronomy & Astrophysics*, 545, A13, doi: [10.1051/0004-6361/201219599](https://doi.org/10.1051/0004-6361/201219599)